Available online at www.sciencedirect.com
ScienceDirect
International Journal of Heat and Mass Transfer 51 (2008) 3776–3793
International Journal of HEAT and MASS TRANSFER
www.elsevier.com/locate/ijhmt

Simulations of the macroscopic and mesoscopic natural convection flows within rectangular cavities

P.-H. Kao, Y.-H. Chen, R.-J. Yang *

Department of Engineering Science, National Cheng Kung University, Tainan 70101, Taiwan

Received 1 October 2007; received in revised form 6 January 2008
Available online 5 March 2008

Abstract

Natural convection within closed cavities is of practical and theoretical interest in many nonlinear sciences and industrial applications. Using a simple lattice Boltzmann (LB) thermal model with the Boussinesq approximation, this study investigates 2D natural convection flows with nonlinear phenomena within enclosed rectangular cavities. The simulations are performed at a constant Prandtl number of $Pr = 0.71$ and the reference Rayleigh numbers of $Ra^* \leqslant 2 \times 10^4$ at the macroscopic scale ($Kn = 10^{-4}$) and the mesoscopic scale ($Kn = 10^{-2}$), respectively. In every case, an appropriate value of the characteristic velocity, i.e. $V \equiv \sqrt{\beta g_y \Delta T H}$, is chosen using a simple model based on the kinetic theory. The simulations commence to identify the convective-dominated stationary, time-independent steady flow (i.e. the primary instability condition). The spectral information of secondary instability with an oscillatory flow is then investigated using a spectrum analysis based on the fast-Fourier transform (FFT) technique. The relationship between the Nusselt number (Nu) and the reference Rayleigh number (Ra^*) is also systematically examined. In general, the simulation results show that unstable flow is generated at particular values of the Rayleigh number, Knudsen number, and cavity aspect ratio. Meanwhile, the Knudsen number and the aspect ratio play key roles in determining the evolution of oscillatory flows beyond the threshold of secondary instability.

Keywords: Natural convection; Mesoscopic flow; Rectangular cavity; Lattice Boltzmann method (LBM); Computational fluid dynamics (CFD)

1. Introduction

The natural convection, or namely the buoyant flow, is the flow motion driven by the temperature or concentration differences interacted with the gravitational effect. Due to its importance in many practical engineering applications and nonlinear sciences, the problem of natural convection within a closed cavity has been the subject of many investigations. Natural convection inside a cavity may make the evolution of a fluid system from a stationary state to a chaotic state characterized by a variety of flow patterns and complex bifurcation sequences. As a result, the transition mechanisms inherent in natural convection are of interest in a wide variety of nonlinear hydrodynamics and industrial applications [1,2].

Previous investigations of natural convection within a cavity have shown that the primary flow instability, which represents a transition from diffusive thermal conduction to a stationary time-independent steady flow structure, occurs at critical Rayleigh numbers in the range $Ra_c = 10^3$–10^4 [3] which is dependent on the cavity aspect ratios. Furthermore, as the Rayleigh number increases, a flow bifurcation to a time-dependent flow motion with a single-frequency periodic oscillatory state is observed, namely the secondary instability. Moreover, as the Rayleigh number is increased yet further in the range of approximately $Ra \approx 10^6$–10^8 [3,4], the flow finally transitions to a chaotic state. de Vahl Davis [1] provided a benchmark numerical solution for a square cavity heated on the left side, cooled on the right side, and with adiabatic boundary conditions on the upper and lower walls. Ostrach [2] investigated natural convection in cavities subject to various boundary conditions and temperature fields. Aydin et al. [5] considered the case

* Corresponding author. Tel.: +886 6 200 2724; fax: +886 6 276 6549.
E-mail address: rjyang@mail.ncku.edu.tw (R.-J. Yang).

0017-9310/$ - see front matter © 2008 Elsevier Ltd. All rights reserved.
doi:10.1016/j.ijheatmasstransfer.2008.01.003

Nomenclature

AR	aspect ratio: AR $\equiv H/L$
c	microscopic particle velocity of the lattice Boltzmann method (LBM)
c_i	microscopic particle velocity in each lattice link i
c_s	speed of sound
f	distribution function for the flow field
f_D	reference thermal diffusive frequency: $f_D \equiv 1/t_D = \alpha/H^2$
f_P	induced oscillatory frequency: $f_P \equiv 1/t_p$
f^*	dimensionless frequency: $f^* \equiv f_P/f_D$
g	distribution function for the temperature field
g_y	acceleration of gravity in the y-direction
H	vertical height of the computational domain
$\dot{J}_i$	momentum input from the buoyant body force in each lattice link i
Kn	Knudsen number
L	horizontal length of the computational domain
N	number of induced harmonic frequencies, and $N \geqslant 2$
Nu	Nusselt number
$\overline{Nu}$	average Nusselt number
Pr	Prandtl number
Ra	Rayleigh number
Ra^*	reference Rayleigh number: $Ra^* \equiv Ra/\mathrm{AR}^3$
Ra_c	critical Rayleigh number for primary instability of natural convection within enclosed cavities
Re	Reynolds number
T	dimensionless temperature within the computational domain
t	computing time-steps in the lattice Boltzmann method (LBM)
t^*	dimensionless time-step: $t^* \equiv t/t_D$
t_D	reference thermal diffusive time scale: $t_D = H^2/\alpha$
t_p	time of period for the induced oscillatory flow
u_A	macroscopic flow velocities in the lattice Boltzmann method (LBM), where sub-index A is the components of Cartesian coordinates
V	characteristic velocity of natural convection, $V \equiv \sqrt{\beta g_y \Delta T H}$

Greek symbols

α	thermal diffusivity
β	expansion coefficient: $\beta \equiv -1/\rho_{\mathrm{ref}}(\partial\rho/\partial T)_P$
λ	mean free path
γ	heat capacity ratio of gas
ΔT	temperature difference
Δt	time interval (step) of LBM
ν	kinetic viscosity
ρ	fluid density
τ_D	relaxation time for the temperature field
τ_v	relaxation time for the flow field

of natural convection in a rectangular enclosure cooled from the ceiling, heated from the left wall and with adiabatic boundary conditions on both the lower and the right walls. Their results indicated that the Nusselt number is strongly dependent on the Rayleigh number when the Rayleigh number is higher than that associated with the threshold of the primary instability, i.e. $Ra > Ra_c$. Ganzarolli and Milanez [6] performed numerical simulations of natural convection within a cavity heated from the bottom, cooled on both sides, and with adiabatic conditions at the upper boundary. The numerical results revealed that a stationary unstable flow with a symmetric structure was formed at a certain value of the Rayleigh number. Furthermore, this value of the Rayleigh number, i.e. the critical Rayleigh number of primary instability (Ra_c), was found to be independent of the Prandtl number. Dalal and Das [7] studied natural convection in cavities of various aspect ratio heated from the bottom wall, and cooled from both side walls and upper boundary. According to their results, the Nusselt number varied as a direct function of the cavity aspect ratio. Sharif and Mohammad [8] investigated natural convection within cavities with different inclination angles and cavity aspect ratios. Their studies focused specifically on the influence of gravitational effects in inducing various unstable flow structures and the effects of the heating length along the lower boundary. Overall, the results of the studies reviewed above indicated that the formation of unstable flow structures in natural convection within enclosed cavities is dependent on the boundary conditions, the aspect ratio (AR) of the cavity, and the direction of gravitational effect. However, the published literature makes little or no reference to the effect of the Knudsen number (e.g. dense or rare gases) on the formation of unstable flow structures in such problems.

The kinetic-based lattice Boltzmann method (LBM) is a powerful numerical technique for simulating fluid flows and modeling the physics in fluids [9–11]. Various numerical simulations have been performed using different thermal LB models or Boltzmann-based schemes to investigate the natural convection problems [12–18]. Although these investigations demonstrated the capability of LB-based models in simulating natural convection, an appropriate model for determining the buoyant velocity scale (V) is still required for mesoscopic flow applications.

The present study employs a simple thermal LB model with the Boussinesq approximation to simulate the instability characteristics of natural convection problems within a closed, rectangular cavity heated from the lower surface and cooled from both the upper boundary and the two side walls. The simulations are performed at different Knudsen numbers at the macroscopic and mesoscopic scales, i.e. $Kn = 10^{-4}$ and $Kn = 10^{-2}$, respectively. A reference Rayleigh

number is defined as $Ra^* \equiv \frac{Ra}{AR^3}$ to be independent of the cavity aspect ratio (AR). It is well known that numerical simulations using the LBM would become inaccurate when flows are associated with strong heat transfer effect (e.g. at high Rayleigh number) or when the flows are away from incompressible regime as reported in Refs. [9,11,13,16,17,19,25]. Based on this reason, the reference Rayleigh number is restricted within $Ra^* \leqslant 2 \times 10^4$ at both the macroscopic and mesoscopic scales. Furthermore, the simulations consider cavities with aspect ratios in the range $0.5 \leqslant AR \leqslant 2.0$ ($AR \equiv H/L$). In every case, the Prandtl number is assumed to be 0.71. Finally, appropriate values of the buoyant characteristic velocity ($V \equiv \sqrt{\beta g_y \Delta T H}$) are determined using a model formulated according to the principles of kinetic theory.

Current simulations commence to identify the flow and cavity geometry conditions under which the initial diffusive thermal conduction transitions to stationary, time-independent flow (i.e. the primary instability). A spectrum analysis based on the fast-Fourier transform (FFT) technique is then performed to identify the time-dependent oscillatory flow frequency associated with the secondary instability. Finally, relationship between the reference Rayleigh number and the buoyancy-induced (natural convective) enhancement of heat transfer (as represented by Nusselt number) is examined.

2. Numerical method

2.1. Lattice Boltzmann model

In investigating the natural convection problem, the effect of viscous heat dissipation can be neglected for applications in incompressible flow [17] such that a simple lattice Boltzmann method can be used in this study. The LB model used here is the same as that employed in [16–18]. The thermal LB model utilizes two distribution functions, f and g, for the flow field and the temperature field, respectively. The density and the temperature distribution functions, i.e. the f and g, are defined as the probability of finding particles at site x at time t moving with the particle velocity c_i during the time interval Δt in each lattice direction (link) i. The two distribution functions obey their respective lattice Boltzmann transport equations with the single relaxation Bhatnagar–Gross–Krook (BGK) approximation, i.e.

$$f_i(x + c_i\Delta t, t + \Delta t) - f_i(x,t) = \frac{\Delta t}{\tau_v}[f_i^{\mathrm{eq}}(x,t) - f_i(x,t)] + \dot{J}_i$$

for the flow field (1)

$$g_i(x + c_i\Delta t, t + \Delta t) - g_i(x,t) = \frac{\Delta t}{\tau_D}[g_i^{\mathrm{eq}}(x,t) - g_i(x,t)]$$

for the temperature field (2)

where $\dot{J}_i$ is the momentum input from the buoyant body force, τ_v and τ_D are the relaxation times for the flow and temperature LB equations, respectively, and $c_s = c/\sqrt{3}$ is the speed of sound. The kinetic viscosity ν and the thermal diffusivity α are defined in terms of their respective relaxation times, i.e. $\nu = c_s^2(\tau_v - 1/2)$ and $\alpha = c_s^2(\tau_D - 1/2)$, respectively. Note that the limitation $0.5 < \tau$ should be satisfied for both relaxation times to ensure that viscosity and thermal diffusivity are positive. Furthermore, the local equilibrium distributions are given by [19]

$$f_i^{\mathrm{eq}}(x,t) = w_i\rho\left[1 + \frac{c_{iA}\cdot u_A}{c_s^2} + \frac{u_A u_B}{2c_s^2}\left(\frac{c_{iA}c_{iB}}{c_s^2} - \delta_{AB}\right)\right]$$

for the flow field (3)

$$g_i^{\mathrm{eq}}(x,t) = w_i\theta\left[1 + \frac{c_{iA}\cdot u_A}{c_s^2} + \frac{u_A u_B}{2c_s^2}\left(\frac{c_{iA}c_{iB}}{c_s^2} - \delta_{AB}\right)\right]$$

for the temperature field (4)

Note that the equilibrium distribution function for the temperature field, i.e. the Eq. (4), can be used at first-order [15,18]. Having computed the values of these local equilibrium functions, the flow properties are defined as

$$\text{Flow density}: \rho = \sum_i f_i \tag{5}$$

$$\text{Momentum}: \rho u_A = \sum_{iA} f_i c_{iA} \tag{6}$$

$$\text{Temperature population}: T = \sum_i g_i \ (0 \leqslant T \leqslant 1) \tag{7}$$

In the equations above, sub-indices A and B denote the components of the Cartesian coordinates with implied summation for repeated indices. Furthermore, w_i is the weighting which can be determined to achieve isotropy of the fourth-order tensor of the velocities and Galilean invariance [19]. Applying the Chapman–Enskog expansion, the continuity equation and the Navier–Stokes equations can be recovered exactly at the second-order approximation from the LB equation of the flow field, i.e. Eq. (1), if the density variation is sufficiently small without the additional body force term $\dot{J}_i$, as derived in [20]

$$\frac{\partial\rho}{\partial t} + \nabla\cdot(\rho\mathbf{u}) = 0 \tag{8}$$

$$\frac{\partial(\rho\mathbf{u}_A)}{\partial t} + \nabla_A\cdot(\rho\mathbf{u}_A\mathbf{u}_B) = -\nabla_A(c_s^2\rho) + \nu\nabla_B\cdot(\nabla_A\rho\mathbf{u}_B + \nabla_B\rho\mathbf{u}_A) \tag{9}$$

Similarly, as derived in [21], the convective–diffusive equation can be obtained from the LB equation of the temperature field given in Eq. (2), i.e.

$$\frac{\partial T}{\partial t} + (\mathrm{u}\cdot\nabla)T = \nabla\cdot(\alpha\nabla T) \tag{10}$$

where T denotes the temperature. In simulating the natural convection problem, the additional buoyant body force term, $\dot{J}_i$, can be formulated by the Boussinesq approximation, i.e.

$$\dot{J}_i = 3w_i\cdot g_y\cdot\beta\cdot T(x,t)\cdot\rho(x,t)\cdot c_{iy} \tag{11}$$

where g_y is the acceleration of gravity acting in the y-direction of the lattice links; β is the thermal expansion coefficient, defined as $\beta \equiv -1/\rho_{\mathrm{ref}}(\partial\ \rho/\partial T)_P$, where ρ_{ref} is the

reference density of the fluid by simply setting $\rho_{ref} = 1$; and c_{iy} is the y-component of c_i. Furthermore, the terms $\rho(x,t)$ and $T(x,t)$, i.e. the dimensionless local density and temperature, are calculated at each lattice site using Eqs. (5) and (6), respectively. Note that this body force term does not affect to the local density of flow but it does change the flow momentum as a result of the buoyancy. Additionally, the results of a previous investigation [16,17] have shown that the simple thermal LB model employed in the current study is applicable to modeling of incompressible thermal flows with negligible viscous dissipation.

To simulate the natural convection problems using the LBM, it is first necessary to determine the characteristic velocity ($V \equiv \sqrt{\beta g_y \Delta T H}$) and then to obtain the corresponding kinetic viscosity (v) and thermal diffusivity (α) through the following relationships involving the Prandtl number and Rayleigh number, respectively:

$$v^2 = \frac{V^2 H^2 Pr}{Ra} \tag{12}$$

and

$$\alpha = \frac{v}{Pr} \tag{13}$$

where $Pr \equiv \frac{v}{\alpha}$ is the Prandtl number, $Ra \equiv \frac{V^2 H^2}{v\alpha}$ is the Rayleigh number, and H denotes the length scale in which the cavity height is chosen for current cases, the relaxation times, τ_v and τ_D, for flow and temperature LB equations given in Eqs. (1) and (2) can then be determined. It implies that both the kinetic viscosity (v) and thermal diffusivity (α) cannot be fixed as constants in LBM simulations if the characteristic velocity (V) is kept constant. Accordingly, Section 2.3 of this paper develops a model for determining appropriate values of the characteristic velocity, V.

The present simulations are based on the D2Q9 model, and hence the relative weightings in Eqs. (3), (4), and (11) are assigned values of $w_i = 4/9$ for $|c_i| = 0$ (for the static particle), $w_i = 1/9$ for $|c_i| = 1$, and $w_i = 1/36$ for $|c_i| = \sqrt{2}$. Regarding the boundary conditions of the flow field, the solid walls are assumed to be no slip, and thus the bounce-back scheme is applied. This scheme specifies the outgoing directions of the distribution functions as the reverse of the incoming directions at the boundary sites. Furthermore, for the temperature field, the local temperature is defined as $T(x,y) = \sum_i g_i(x,y)$ in Eq. (7) and the no-slip condition ($u_x = u_y = 0$) is applied at all of the solid nodes. Consequently, the treatment of the temperature population (i.e. the distribution function g) at the adiabatic walls can be simplified by applying the bounce-back scheme to the temperature distribution function g_i such that a "heat flux-free state" is obtained in each lattice direction for the specific nodes associated with the adiabatic boundary condition, i.e. $\dot{q}_i = \partial T_i/\partial x_i = (g_i - g_{-i})/\Delta x = 0$. Moreover, the local equilibrium distribution for the temperature field at the thermal wall with a constant temperature can be given by Eq. (4).

2.2. Dimensionless frequency

The present simulations employ the following dimensionless frequency to quantify the oscillatory flow frequency generated within the enclosed cavity. The dimensionless frequency, i.e. f^*, is defined as

$$f^* \equiv \frac{f_P}{f_D} = \frac{H^2}{\alpha \cdot t_p} \tag{14}$$

where f_P is the oscillatory frequency of the flow induced by thermal convection, i.e. $f_P = \frac{1}{t_p}$, in which t_p is the period of the oscillatory flow, and f_D is the reference thermal diffusive frequency, defined as $f_D = \frac{\alpha}{H^2}$. However, the reciprocal of the dimensionless frequency represents the ratio of the oscillatory time scale to the diffusive time scale, i.e. $f^* = \frac{t_D}{t_p}$. Therefore, the dimensionless frequency given in Eq. (14) is meaningless for stationary convection flow since $t_p = 0$. From the definition of the dimensionless frequency, it is apparent that the oscillatory flow moves more rapidly as the value of the dimensionless frequency increases. In general, the value of f^* computed in the LB simulations provides a convenient way of obtaining the value of t_p for practical engineering applications.

To determine the dimensionless frequency f^* via spectrum analysis, the following dimensionless time-step t^* is introduced:

$$t^* \equiv \frac{t'}{t_D} \tag{15}$$

where t' is the number of time-steps in LB simulation, and t_D is the diffusive time scale described above. For practical engineering applications, a heat-flow meter with chart-recorder can be used to measure unsteady heat flux. The frequency of this unsteady heat flux, therefore, can be analyzed. Based on the definition depicted in Eq. (23), the simulated total heat flux is approximately equal to $Nu \cdot \alpha \cdot \Delta T/H$. Accordingly, the unsteady Nusselt values of the oscillatory flow can then be utilized instead of the measured heat flux signal for FFT spectrum analysis in the present LB simulations.

2.3. Model for determining the appropriate value of buoyant characteristic velocity in LBM simulations for natural convection problems

Choosing an appropriate value of the characteristic velocity ($V \equiv \sqrt{\beta g_y \Delta T H}$) is essential when simulating natural convection problems using Boussinesq approximation. However, there are no theoretical criteria available for determining appropriate values of V for different natural convection problems, and hence a value is generally chosen by the empirical test in numerical simulations. To overcome this difficulty, the present study develops a model for determining an appropriate characteristic velocity value based on the principle of kinetic theory. According to kinetic theory [22,23], the Knudsen number has the form [24]

$$Kn = \sqrt{\frac{\pi\gamma}{2}} \cdot \frac{Ma}{Re} \tag{16}$$

where Ma is the Mach number, Re is the Reynolds number, and the heat capacity ratio to be $\gamma = 5/3$ for a monatomic ideal gas and $\gamma = 7/5$ for a diatomic gas. Eq. (16) implies that the mean free path can be written as $\lambda = \sqrt{\frac{\pi\gamma}{2}}\frac{v}{c_s}$. As a result, the Knudsen number for the current natural convection case can be written as

$$Kn \equiv \frac{\lambda}{H} = \sqrt{\frac{\pi\gamma}{2}} \cdot \frac{v}{c_s \cdot H} \tag{17}$$

According to the definition of Rayleigh number, the Rayleigh number also has the form:

$$Ra = \frac{V^2 H^2}{v^2} \cdot Pr \tag{18}$$

Therefore, an expression for V^2 can be formulated by combining the squared Eq. (17): $Kn^2 = \frac{\pi\gamma v^2}{2c_s^2 H^2}$ and Eq. (18) to get

$$V^2 = \frac{Ra \cdot Kn^2 \cdot c_s^2}{\pi\gamma Pr/2}, \text{ where } c_s^2 = \frac{c^2}{3} \tag{19}$$

In other words, the characteristic velocity is a function of the Rayleigh number, Knudsen number, Prandtl number, and the value of γ, all of which are specified as given values in LBM simulations. Eq. (19), therefore, provides the means to determine an appropriate value of the buoyant velocity for LBM in simulating natural convection problems at both the macroscopic and the mesoscopic scales.

Importantly, the value assigned to the characteristic velocity (V) should satisfy the incompressible limit as reported in [13,16,17]. This incompressible condition requires the flows to have a small Mach number, i.e. $Ma \equiv U_{avg}/c_s$, where U_{avg} is the buoyancy-induced average velocity throughout domain and is governing by the specified value of the characteristic velocity (V). As a result, larger values of V may lead to computational instability of the numerical model, resulting in inaccurate simulation results. The relationship between V and U_{avg} depends on the numerical model applied, the boundary conditions, the grid size, and the specific geometry of the domain in natural convection problems under investigation. However, no literature is available to discuss the relationship between V and U_{avg} for various problems of natural convection with complex flow instability phenomena. Accordingly, the current simulations deliberately restrict the range of the Rayleigh number in order to ensure compliance with the incompressible condition.

3. Validation of characteristic velocity model

The characteristic velocity model given in Eq. (19) was validated for the problem of natural convection within a 2D square cavity by performing a grid-independent study. An assumption was made that the initial stationary flow was heated from the left wall, i.e. $T_{Left} = 1$, while the right wall was maintained at a constant low temperature, i.e. $T_{right} = 0$. Meanwhile, the upper and bottom boundary walls were assigned adiabatic boundary conditions. A vertical gravitational effect was applied in the y-direction. Regarding the flow field, the square cavity was assumed to be closed and the no-slip boundary conditions were imposed at each of the four solid walls. Finally, the initial conditions within the computational domain were specified as: $T(x,y) = 0$, $u_x(x,y) = u_y(x,y) = 0$, and a uniform density of $\rho(x,y) = 1$.

The simulations were based on the D2Q9 (two-dimensional, nine-velocity) model and an assumption was made that the 2D cavity had an aspect ratio of AR = 1. The computational domain was mapped using a square lattice, i.e. $\Delta x = \Delta y$, and the simulations were performed using a variety of grid systems, namely 41×41, 81×81 and 161×161, respectively. The Prandtl number ($Pr \equiv v/\alpha$) was assumed to have a constant value of 0.71 in every case. Meanwhile, the definitions of the Rayleigh number (Ra) and the Nusselt number (Nu) were given as

$$Ra = \frac{\beta \cdot \Delta T \cdot g_y \cdot L^3}{v\alpha} \tag{20}$$

and

$$Nu = 1 + \frac{\langle u_x \cdot T \rangle}{\alpha \cdot \Delta T/L} \tag{21}$$

where L is the horizontal length of the closed cavity, $\Delta T = 1$ is fixed and represents the temperature difference between the left and right boundaries, and $\langle\rangle$ denotes the average value over the whole domain.

In the validation simulations, appropriate values of V were obtained using the model presented in Eq. (19) with a fixed Knudsen number of $Kn = 10^{-4}$ at the macroscopic scale and Rayleigh numbers of $Ra = 10^3$, 10^4, 10^5 and 10^6, respectively. Table 1 presents the value of V and the Nusselt number computed at each Rayleigh number using the

Table 1
Comparison of Nusselt numbers computed at different Rayleigh numbers using different grids with results presented in [1]

Ra:	10^3	10^4	10^5	10^6
Nu by de Vahl Davis, 1983 [1]	1.118	2.243	4.519	8.825
Nu by present LBM				
Used V value according to Eq. (14)	2.134×10^{-6}	2.134×10^{-5}	2.134×10^{-4}	2.134×10^{-3}
Grid: 41×41	1.106 (1.07%)	2.207 (1.60%)	4.420 (2.19%)	8.406 (4.48%)
Grid: 81×81	1.113 (0.45%)	2.231 (0.54%)	4.488 (0.69%)	8.696 (1.18%)
Grid: 161×161	1.115 (0.24%)	2.238 (0.24%)	4.506 (0.28%)	8.769 (0.35%)

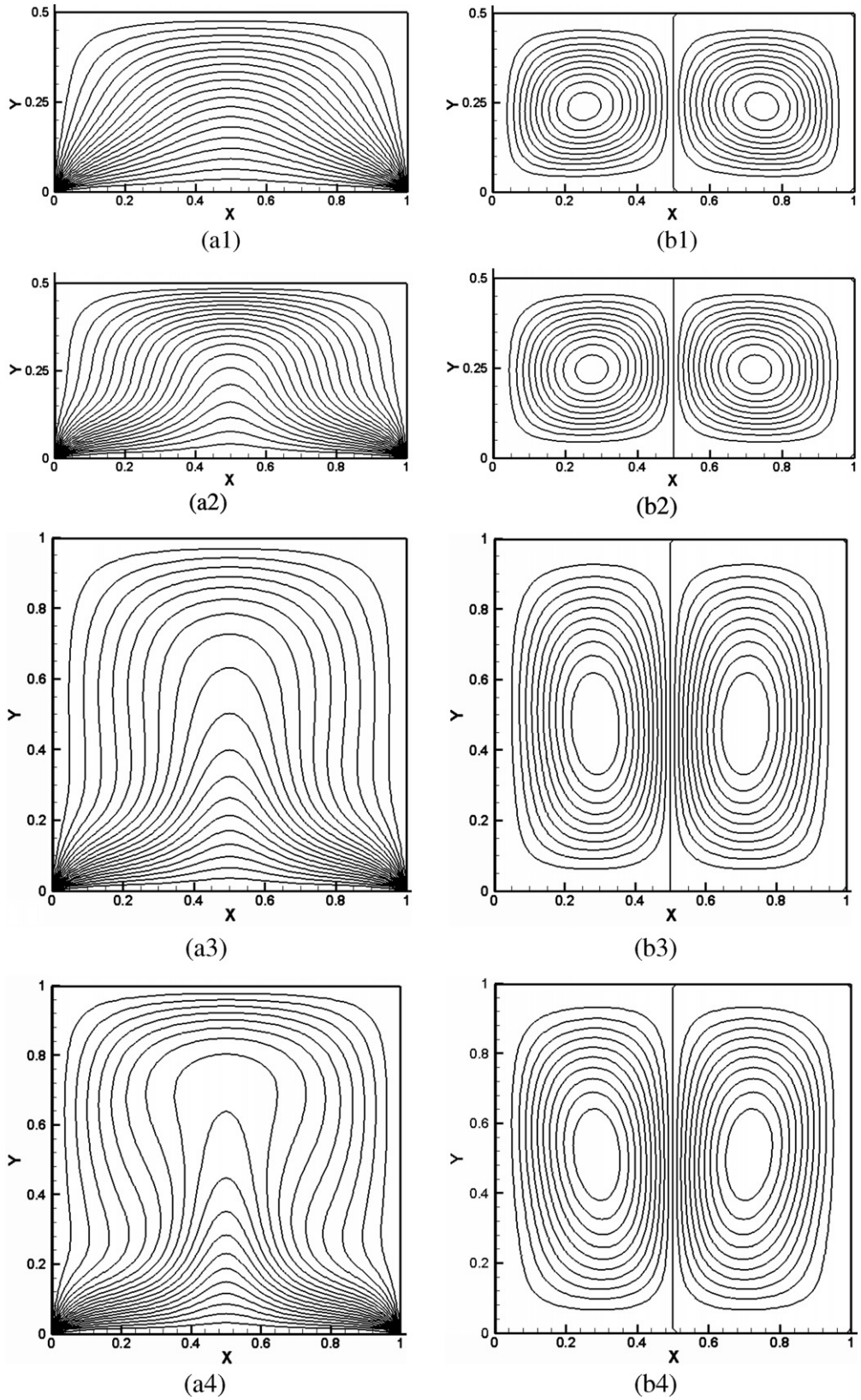

Fig. 1. Steady temperature and stream function contours at macroscopic scale ($Kn = 10^{-4}$) in different cavities with aspect ratios from AR = 0.5 to AR = 1.5, $Pr = 0.71$, and various Ra^*: (a1) AR=0.5: temperature contours at $Ra^* = 10^3$, (a2) AR = 0.5: temperature contours at $Ra^* = 2 \times 10^4$, (a3) AR = 1.0: temperature contours at $Ra^* = 10^3$, (a4) AR = 1.0: temperature contours at $Ra^* = 2 \times 10^4$, (a5) AR = 1.5: temperature contours at $Ra^* = 10^3$, and (a6) AR = 1.5: temperature contours at $Ra^* = 2 \times 10^4$; (b1) AR = 0.5: stream function contours at $Ra^* = 10^3$, (b2) AR = 0.5: stream function contours at $Ra^* = 2 \times 10^4$, (b3) AR = 1.0: stream function contours at $Ra^* = 10^3$, (b4) AR = 1.0: stream function contours at $Ra^* = 2 \times 10^4$, (b5) AR = 1.5: stream function contours at $Ra^* = 10^3$, and (b6) AR = 1.5: stream function contours at $Ra^* = 2 \times 10^4$.

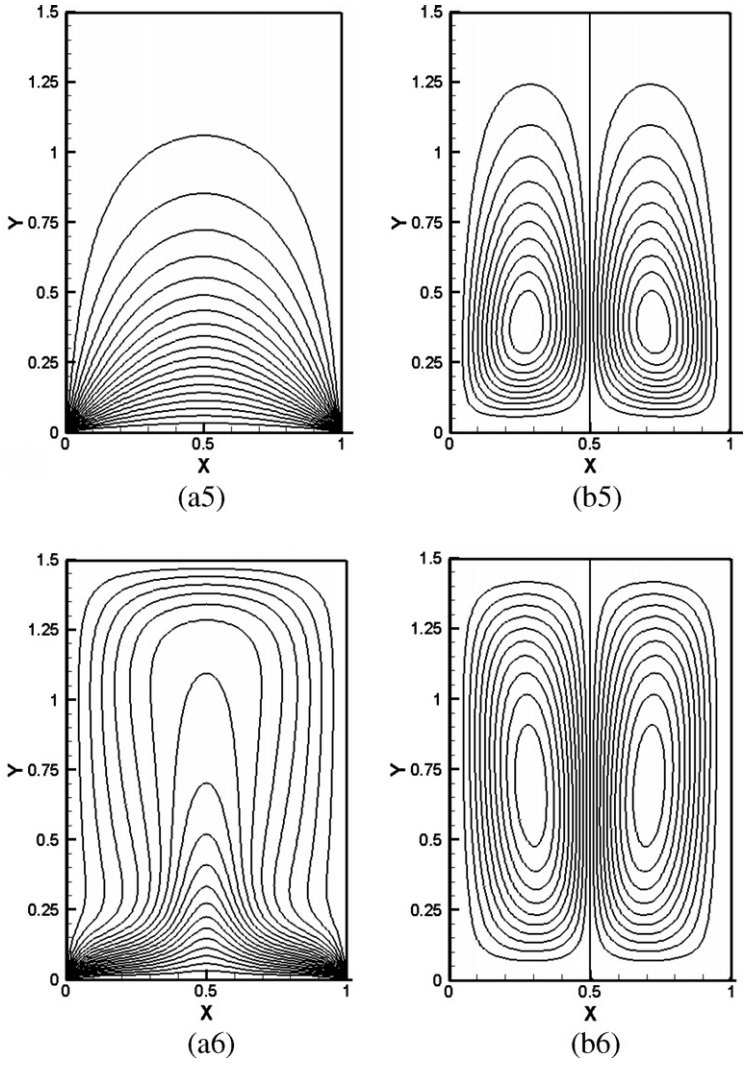

Fig. 1 (*continued*)

three different grid systems. The present results are compared with those presented in [1] for validation purposes. The current results are similar to those presented in [15–17,25,26]. The percentage data given in parentheses indicate the deviation of the current simulation results from the solutions presented in [1]. When performing the simulations using a grid size of 81×81 or 161×161, the discrepancy between the two sets of results is less than 2%. Even when using the coarsest grid, i.e. 41×41, the error is still less than 5%. Overall, the simulation results confirm the feasibility of using the current LB scheme and characteristic velocity model to investigate natural convection problems at the macroscopic scale.

4. Simulations of natural convection within closed rectangular cavities

The present simulations employ a simple thermal LB model with the Boussinesq approximation for the buoyant body force term and a characteristic velocity model to investigate the 2D natural convection inside a closed cavity at different reference Rayleigh numbers $Ra^* \leqslant 2 \times 10^4$, in which $Ra^* \equiv Ra/\mathrm{AR}^3$ is defined to be independent of the cavity aspect ratio (AR), at both the macroscopic scale ($Kn = 10^{-4}$) and the mesoscopic scale ($Kn = 10^{-2}$), respectively. In every case, the Prandtl number is assumed to be 0.71. The geometry effect is investigated by repeating the simulations at various values of the cavity aspect ratio, i.e. $\mathrm{AR} \equiv H/L = 0.5$, 1.0, 1.5 and 2.0, respectively. The instability phenomena associated with the resulting oscillatory flow frequencies are then investigated using a fast-Fourier transform (FFT) technique, with 2^{17} dimensionless time-steps (i.e. t^* in Eq. (15)). Finally, the relationship between the Nusselt number and the reference Rayleigh number is systematically examined as a function of the aspect ratio and the Knudsen number.

The present simulations were based on the D2Q9 model in which the 2D cavity was meshed using a square lattice. In accordance with the validation results presented in Section 3, each unit length of the computational domain, i.e. $L = 80 \cdot \Delta x$ for the lower boundary, was mapped using 81 grid nodes. The number of grid points in the vertical

direction (i.e. height H) of the cavity was then determined by the aspect ratio ($AR \equiv H/L$) considered in the particular simulation. In modeling the flow field, all four solid boundaries were assigned no-slip conditions. Meanwhile, in simulating the temperature field, the lower wall was assigned a constant temperature of $T_{Bottom} = 1$, while the other three walls were each assigned a constant, low temperature, i.e. $T_{Upper} = T_{Left} = T_{Right} = 0$, respectively. The initial conditions within the domain were specified as: $T(x, y) = 0$, $u_x(x, y) = u_y(x, y) = 0$, and a uniform density

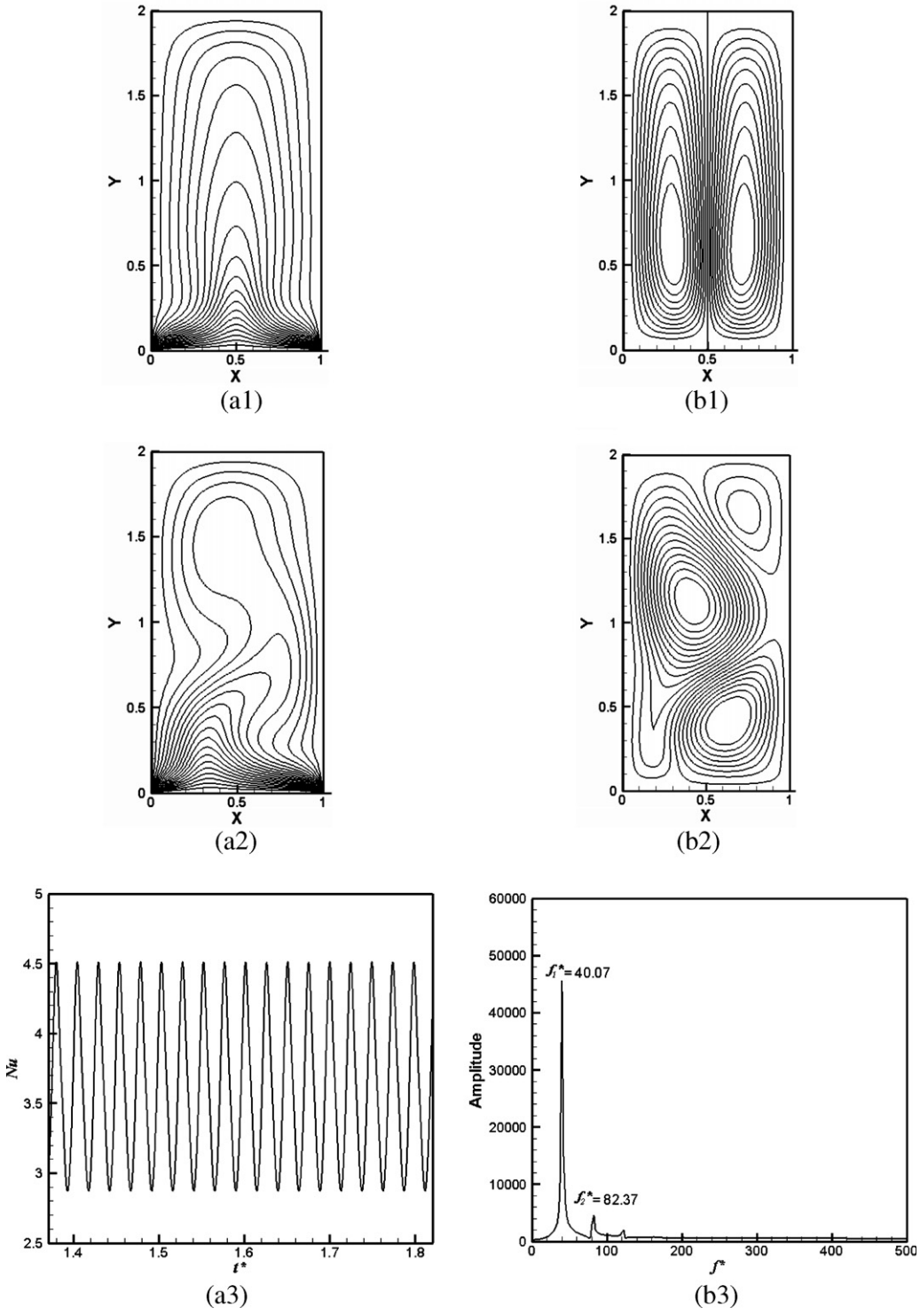

Fig. 2. Temperature and stream function contours at macroscopic scale ($Kn = 10^{-4}$) for stationary and oscillatory unstable flows in cavity with aspect ratio of AR = 2.0, $Pr = 0.71$, and various Ra^*: (a1) temperature contours in stationary state at $Ra^* = 1.5 \times 10^4$, (a2) temperature contours of oscillatory flow at $Ra^* = 2 \times 10^4$ and time-step $= 6 \times 10^6$, and (a3) FFT spectrum analysis results for variation of Nusselt number with dimensionless time-step at $Ra^* = 2 \times 10^4$; (b1) stream function contours in stationary state at $Ra^* = 1.5 \times 10^4$, (b2) stream function contours of oscillatory flow at $Ra^* = 2 \times 10^4$ and time-step $= 6 \times 10^6$, and (b3) FFT spectrum analysis results for relationship between dimensionless frequency and oscillatory amplitude at $Ra^* = 2 \times 10^4$.

of $\rho(x,y)=1$. Finally, the Rayleigh number and Nusselt number definitions were revised to

$$Ra=\frac{\beta\cdot\Delta T\cdot g_y\cdot H^3}{v\alpha} \tag{22}$$

and

$$Nu=1+\frac{\langle u_y\cdot T\rangle}{\alpha\cdot\Delta T/H} \tag{23}$$

where H is the vertical height of the cavity, $\Delta T=1$ is constant and denotes the temperature difference between the upper and bottom boundaries. Note that in the case of unsteady flow, the Nusselt data presented in this study represent time-averaged values (i.e. $\overline{Nu}$).

As described previously, the buoyant velocity scale considered in the present simulations was determined via the model given in Eq. (19). Rearranging Eq. (19), the Rayleigh number can be written as $Ra=\frac{V^2\cdot\pi\gamma\cdot Pr}{2\cdot Kn^2\cdot c_s^2}$, where $V^2=\beta g_y\Delta T\,H$ and $Kn^2=\pi\gamma/2H^2\cdot v^2/c_s^2$, and the height of the cavity can be written as $H=\mathrm{AR}\cdot L$. If a reference Rayleigh number is defined as $Ra^*\equiv\left(Pr\cdot\frac{V^2H^2}{v^2}\right)_{H=L}$, the characteristic velocity model can then be reformulated as

$$V^2=\mathrm{AR}^3\frac{Ra^*\cdot Kn^2\cdot c_s^2}{\pi\gamma Pr/2},\quad \text{where } \mathrm{AR}\equiv\frac{H}{L} \tag{24}$$

where the Kn, AR, and $Ra^*=\frac{Ra}{\mathrm{AR}^3}$ are all specified as the given values. The following simulations performed in this study are all based on this revised characteristic velocity model given by Eq. (24). However, it should be noted that the higher value of V may break the incompressible condition described in Section 2.3. Consequently, the reference Rayleigh numbers considered in the current simulations are deliberately restricted to the range $Ra^*\leqslant 2\times10^4$ at both the macroscopic scale ($Kn=10^{-4}$) and the mesoscopic scale ($Kn=10^{-2}$).

4.1. Natural convection within cavities at macroscopic scale ($Kn=10^{-4}$)

The simulations commenced by investigating the characteristics of 2D natural convection at the macroscopic scale ($Kn=10^{-4}$) within closed cavities with aspect ratios ranging from $\mathrm{AR}=0.5$ to 2.0. Fig. 1 presents the simulated temperature and stream function contours in cavities with aspect ratios of $\mathrm{AR}=0.5$, 1.0 and 1.5, respectively, at reference Rayleigh numbers of $Ra^*=10^3$ and $Ra^*=2\times10^4$. Overall, the results demonstrate that the flow conditions considered in these particular simulations, i.e. $Ra^*\leqslant 2\times10^4$, $0.5\leqslant\mathrm{AR}\leqslant1.5$ and $Pr=0.71$, generate only symmetric stationary unstable flows (i.e. a primary instability) at the macroscopic scale, i.e. no bifurcation to secondary instability occurs. As shown in Figs. 1(a2), (a4) and (a6), when the aspect ratio of the cavity is increased (from $\mathrm{AR}=0.5$ to $\mathrm{AR}=1.5$) at higher values of the reference Rayleigh number, the length of the "finger structure" in the temperature contours also increases, since the larger AR value provides the longer space of H to develop the finger structure along the y-direction which denotes the direction for heat transfer in present cases, i.e. $H_{\mathrm{AR}=1.5}>H_{\mathrm{AR}=0.5}$. When the flow state contains a longer finger structure, the initial symmetric, stationary flow becomes unstable when a small perturbation is introduced. This may cause the symmetric flow structure to be broken and transitions to secondary instability with an unsteady oscillatory flow. Note that the small perturbation is self-induced during the calculation when the flow is at higher Rayleigh number, i.e. no artificial perturbation is required for LB simulations in present cases.

When the aspect ratio is increased to $\mathrm{AR}=2.0$, the length of the finger structure in the temperature contours is far longer than that in a cavity with a lower aspect ratio. As a result, the initial symmetric, stationary flow becomes unstable when any small perturbation is generated, prompting a transition to secondary instability conditions with an unsteady oscillatory flow state. Fig. 2 presents the steady and unsteady solutions of the temperature and stream function contours at the macroscopic scale and the FFT spectrum analysis of the oscillatory flows. The results indicate that secondary instability occurs at reference Rayleigh numbers of approximately $Ra^*=1.5\times10^4$–2×10^4 in an enclosed cavity with an aspect ratio of $\mathrm{AR}=2.0$. Figs. 2(a3) and (b3) show that a single-frequency oscillatory flow with a dimensionless frequency of $f_1^*=40.07$ is generated at $Ra^*=2.0\times10^4$. Meanwhile, only one harmonic frequency with a value of $f_2^*=82.37$ with an amplitude value far smaller than the amplitude of the dominant frequency (f_1^*) when $Ra^*\leqslant 2\times10^4$ is formed at the macroscopic scale.

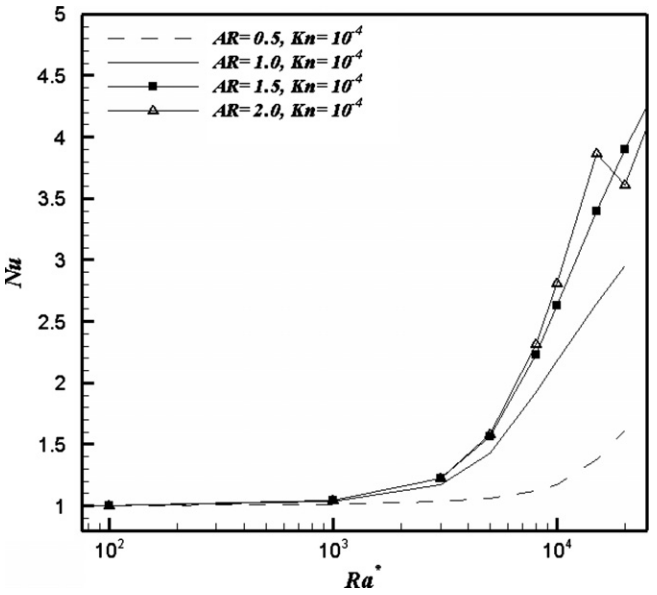

Fig. 3. Variation of Nusselt number with reference Rayleigh number at macroscopic scale ($Kn=10^{-4}$) for cavities with aspect ratios in the range $0.5\leqslant\mathrm{AR}\leqslant2.0$, $Pr=0.71$, and $Ra^*\leqslant2\times10^4$.

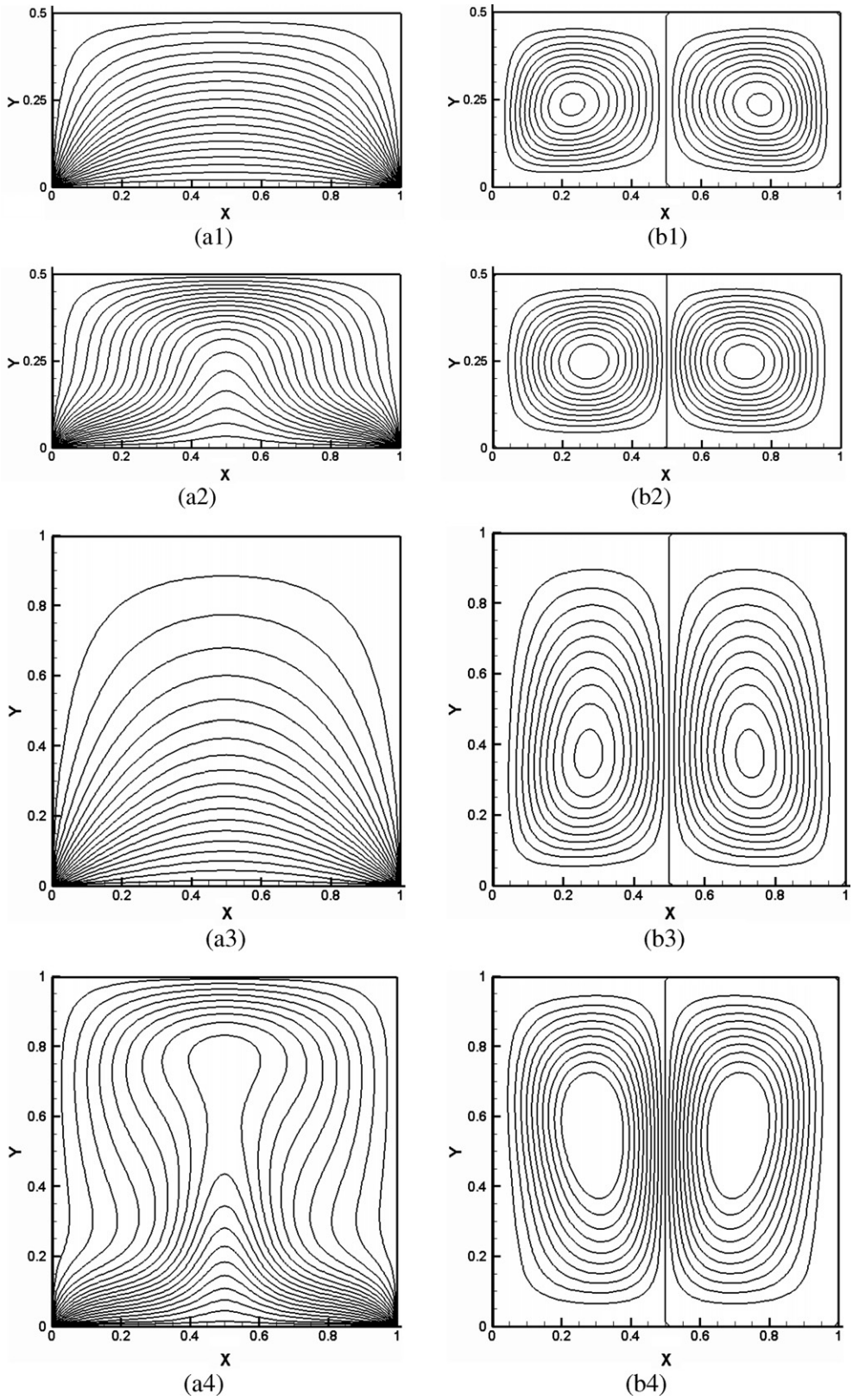

Fig. 4. Steady temperature and stream function contours at mesoscopic scale ($Kn = 10^{-2}$) in different cavities with aspect ratios from AR = 0.5 to AR = 1.0, $Pr = 0.71$, and various Ra^*: (a1) AR = 0.5: temperature contours at $Ra^* = 10^3$, (a2) AR = 0.5: temperature contours at $Ra^* = 2 \times 10^4$, (a3) AR = 1.0: temperature contours at $Ra^* = 10^3$, and (a4) AR = 1.0: temperature contours at $Ra^* = 2 \times 10^4$; (b1) AR = 0.5: stream function contours at $Ra^* = 10^3$, (b2) AR = 0.5: stream function contours at $Ra^* = 2 \times 10^4$, (b3) AR = 1.0: stream function contours at $Ra^* = 10^3$, and (b4) AR = 1.0: stream function contours at $Ra^* = 2 \times 10^4$.

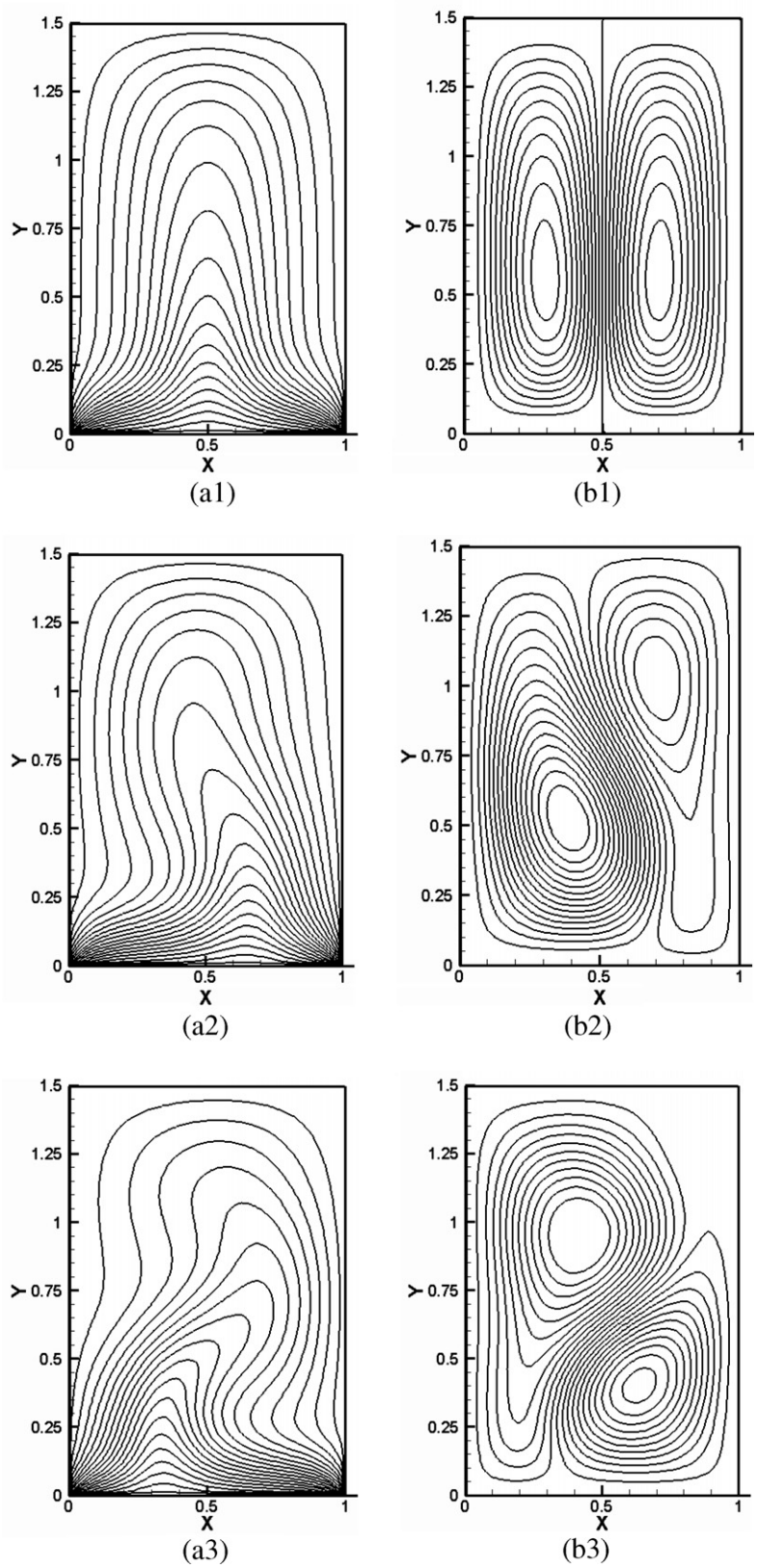

Fig. 5. Temperature and stream function contours at mesoscopic scale ($Kn = 10^{-2}$) for stationary and oscillatory unstable flows in cavity with aspect ratio of AR = 1.5, $Pr = 0.71$, and various Ra^*:(a1) temperature contours in stationary state at $Ra^* = 8 \times 10^3$, (a2) temperature contours of oscillatory flow at $Ra^* = 8.5 \times 10^3$ and time-step $= 2 \times 10^5$, (a3) temperature contours of oscillatory flow at $Ra^* = 1.5 \times 10^4$ and time-step $= 7 \times 10^4$, and (a4) temperature contours of oscillatory flow at $Ra^* = 2 \times 10^4$ and time-step $= 5 \times 10^4$; (b1) stream function contours in stationary state at $Ra^* = 8 \times 10^3$, (b2) stream function contours of oscillatory flow at $Ra^* = 8.5 \times 10^3$ and time-step $= 2 \times 10^5$, (b3) stream function contours of oscillatory flow at $Ra^* = 1.5 \times 10^4$ and time-step $= 7 \times 10^4$, and (b4) stream function contours of oscillatory flow at $Ra^* = 2 \times 10^4$ and time-step $= 5 \times 10^4$.

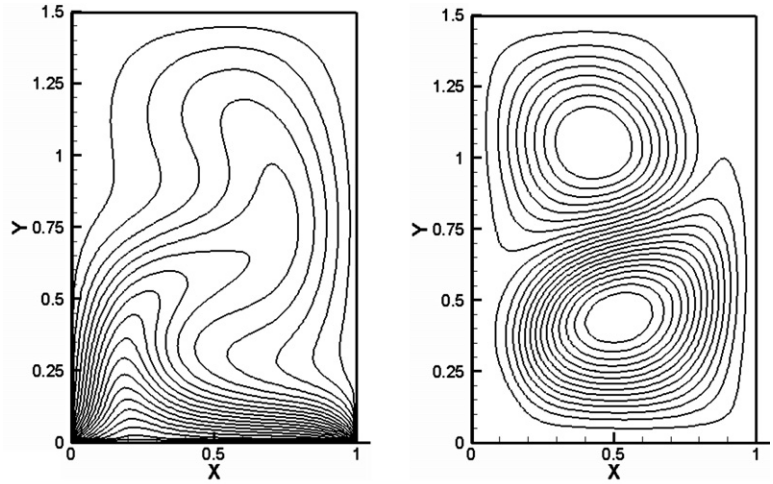

Fig. 5 (*continued*)

Fig. 3 illustrates the variation of the Nusselt number within $Ra^* \leqslant 2 \times 10^4$ at the macroscopic scale ($Kn = 10^{-4}$) as a function of the aspect ratio. It is evident that both the cavity aspect ratio and the Rayleigh number play key roles in determining the onset of flow instability. The primary instability condition occurs at actual Rayleigh numbers between $Ra = 10^3$ and 10^4, with the exact value determined by the aspect ratio. The results confirm that secondary instability with an unsteady oscillatory flow is formed at the macroscopic scale only in enclosed cavities with aspect ratios of AR = 2.0 and $Ra^* \leqslant 2 \times 10^4$. In general, it can be seen that the value of the Nusselt number increases with increasing reference Rayleigh number and increasing aspect ratio.

4.2. Natural convection within cavities at mesoscopic scale ($Kn = 10^{-2}$)

The second set of simulations performed in the current study was designed to investigate the problem of 2D natural convection within closed cavities at the mesoscopic scale ($Kn = 10^{-2}$). As before, an appropriate value of the buoyant characteristic velocity was determined using the model given in Eq. (24) and the flow simulations were deliberately restricted to the reference Rayleigh number $Ra^* \leqslant 2 \times 10^4$.

Fig. 4 presents the temperature and stream function contours at $Ra^* = 10^3$ and 2×10^4, respectively, for enclosed cavities with aspect ratios of AR = 0.5 and AR = 1.0. Overall, the results indicate that at the mesoscopic scale, these flow and geometry conditions result in the formation only of stationary primary instability flow with a symmetric flow structure. In other words, no bifurcation to secondary instability flow takes place when $Ra^* \leqslant 2 \times 10^4$, AR = 0.5, and AR = 1.0.

Figs. 5 and 6 illustrate the steady and unsteady temperature contours, stream function contours, and the FFT spectrum analysis results for the corresponding oscillatory flows, respectively, in a cavity with an aspect ratio of AR = 1.5. As shown in Fig. 5, secondary instability with an unsteady oscillatory flow is generated at reference Rayleigh numbers within the range $Ra^* = 8 \times 10^3$ to 8.5×10^3. It should be noted that secondary instability was found at the macroscopic scale only in a cavity with AR = 2.0 within $Ra^* \leqslant 2 \times 10^4$. In general, the results presented in Figs. 5 and 6 show that as the reference Rayleigh number increases toward $Ra^* \leqslant 2 \times 10^4$, the initial stationary unstable flow transitions to a symmetry-breaking oscillatory flow structure via the frequency doubling route. However, the dominant frequency is insensitive to the increasing reference Rayleigh number and remains constant at $f_1^* \approx 10$. Furthermore, period flow motion with doubly harmonic frequencies relationship are approximately satisfied, i.e. $f_N^* \approx f_1^* \cdot N$ where N is the number of induced harmonic frequencies and $N \geqslant 2$.

Fig. 7 presents the temperature and stream function contours at the mesoscopic scale in a cavity with an increased aspect ratio of AR = 2.0 for reference Rayleigh numbers of $Ra^* = 6 \times 10^3$, 6.5×10^3, 10^4, and 2×10^4, respectively. Fig. 8 illustrates the corresponding FFT spectrum analysis results. The figures reveal that secondary instability flow is generated at the reference Rayleigh number of approximately $Ra^* = 6 \times 10^3$–6.5×10^3. This value is slightly lower than that observed in the cavity with a lower aspect ratio of AR = 1.5. However, the dominant frequency of the oscillatory flow, i.e. $f_1^* = 12$–13, is similar to that found in the lower aspect ratio case. Fig. 8 shows that when $Ra^* \leqslant 1.8 \times 10^4$, the oscillatory flow with doubly harmonic frequencies relationship are approximately satisfied and the number of harmonic frequencies increases with increasing Rayleigh number. At $Ra^* \leqslant 1.5 \times 10^4$, the amplitude of the dominant oscillatory frequency (f_1^*) is larger than that of the induced harmonic frequencies (f_N^*, where $N \geqslant 2$). However, at a reference Rayleigh number

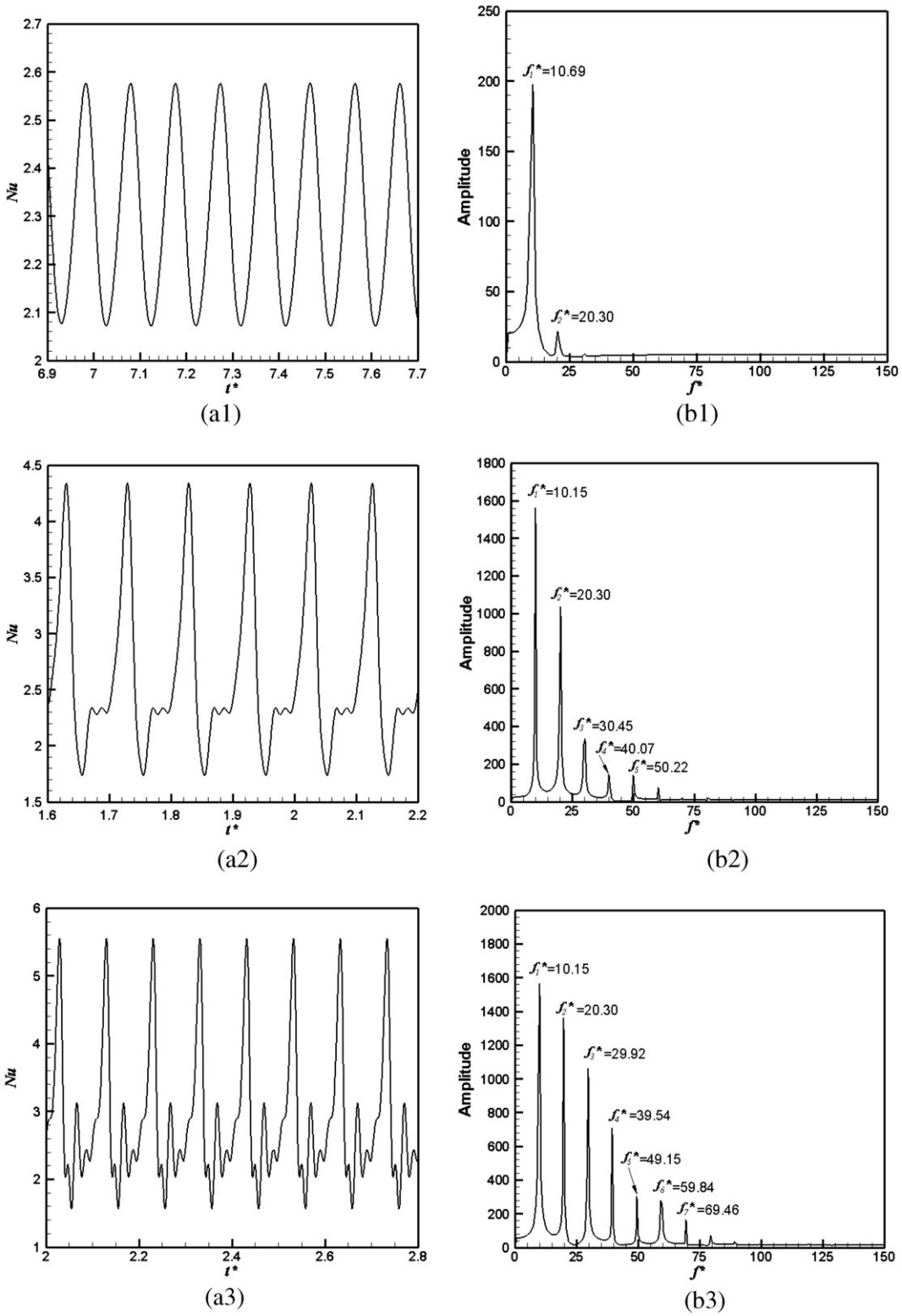

Fig. 6. FFT spectrum analysis results for oscillatory unstable flows at mesoscopic scale ($Kn = 10^{-2}$) in cavity with aspect ratio of AR = 1.5, $Pr = 0.71$, and various Ra^*: (a1) variation of Nusselt number with dimensionless time-step at $Ra^* = 8.5 \times 10^3$, (a2) variation of Nusselt number with dimensionless time-step at $Ra^* = 1.5 \times 10^4$, and (a3) variation of Nusselt number with dimensionless time-step at $Ra^* = 2 \times 10^4$; (b1) relationship between dimensionless frequency and oscillatory amplitude at $Ra^* = 8.5 \times 10^3$, (b2) relationship between dimensionless frequency and oscillatory amplitude at $Ra^* = 1.5 \times 10^4$, and (b3) relationship between dimensionless frequency and oscillatory amplitude at $Ra^* = 2 \times 10^4$.

of $Ra^* = 1.8 \times 10^4$, the oscillatory amplitude of the primary dominant frequency f_1^* is lower than that of some of the induced harmonic frequencies, as shown in Fig. 8(b4). Finally, when the reference Rayleigh number

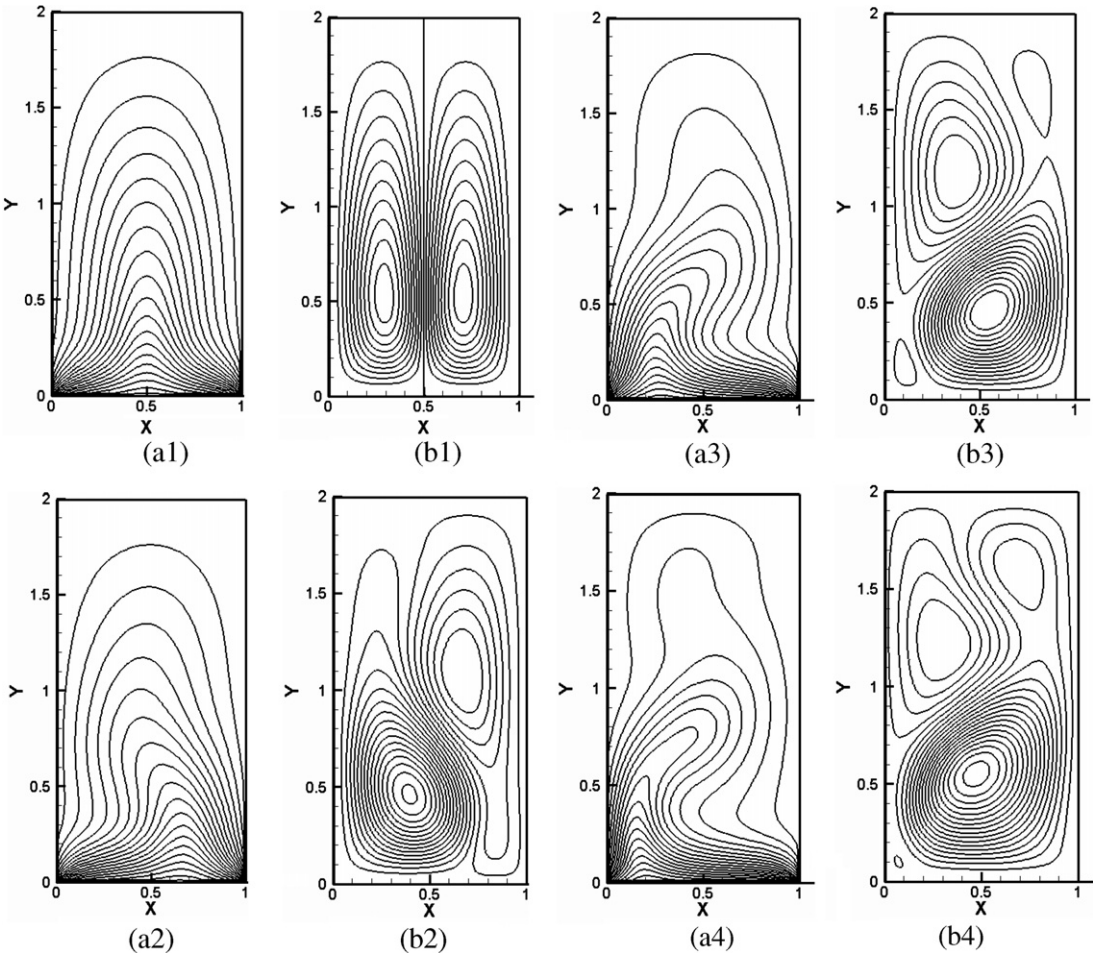

Fig. 7. Temperature and stream function contours at mesoscopic scale ($Kn = 10^{-2}$) for stationary and oscillatory unstable flows in cavity with aspect ratio of AR = 2.0, $Pr = 0.71$, and various Ra^*: (a1) temperature contours in stationary state at $Ra^* = 6 \times 10^3$, (a2) temperature contours of oscillatory flow at $Ra^* = 6.5 \times 10^3$ and time-step $= 1.5 \times 10^5$, (a3) temperature contours of oscillatory flow at $Ra^* = 10^4$ and time-step $= 6 \times 10^4$, and (a4) temperature contours of oscillatory flow at $Ra^* = 2 \times 10^4$ and time-step $= 6 \times 10^4$; (b1) stream function contours in stationary state at $Ra^* = 6 \times 10^3$, (b2) stream function contours of oscillatory flow at $Ra^* = 6.5 \times 10^3$ and time-step $= 1.5 \times 10^5$, (b3) stream function contours of oscillatory flow at $Ra^* = 10^4$ and time-step $= 6 \times 10^4$, and (b4) stream function contours of oscillatory flow at $Ra^* = 2 \times 10^4$ and time-step $= 6 \times 10^4$.

is increased further to $Ra^* = 2.0 \times 10^4$, the amplitude of the noise induced by the flow perturbation increases significantly and causes the flow transitions to a near-chaotic state as exhibited in Fig. 8(b5).

Fig. 9 presents the variation of the Nusselt number with the reference Rayleigh number over the $Ra^* \leqslant 2 \times 10^4$ at the mesoscopic scale. As observed in Fig. 3 for the macroscopic scale, it can be seen that the Rayleigh number and the aspect ratio both play significant roles in determining the onset of unstable flow and the value of the Nusselt number at the mesoscopic scale. In general, the reference Rayleigh number associated with secondary unstable flow reduces as the aspect ratio increases. Furthermore, for a constant aspect ratio, the Nusselt number increases with increasing reference Rayleigh number. Additionally, prior to the onset of secondary instability, the Nusselt number also increases with increasing aspect ratio at a constant reference Rayleigh number. Overall, the results presented in Fig. 9 show that the onset of primary instability is relatively insensitive to the aspect ratio and occurs at reference Rayleigh numbers in the range of $Ra^* = 10^3$–10^4 in every case. In this sense, the current results are consistent with those presented at the macroscopic scale in Fig. 3, however, the onset of secondary instability is strongly dependent on the aspect ratio. In the cases of AR = 1.5 and 2.0, respectively as shown in Fig. 9, it can be seen that there is a significant reduction in the slope of the Nu–Ra^* curves after the onset of secondary instability. In other words, it can be inferred that unsteady (secondary) unstable flow fails to yield an effective enhancement in the heat transfer effect of natural convection systems within enclosed cavities with aspect ratios in the range $1.5 \leqslant \mathrm{AR} \leqslant 2.0$.

4.3. Comparison of results at macroscopic and mesoscopic scales

Fig. 10 illustrates the variation of the Nusselt number with the reference Rayleigh number at both the macroscopic and the mesoscopic scales in cavities with aspect ratios ranging from AR = 0.5 to AR = 2.0 and $Ra^* \leqslant 2 \times$

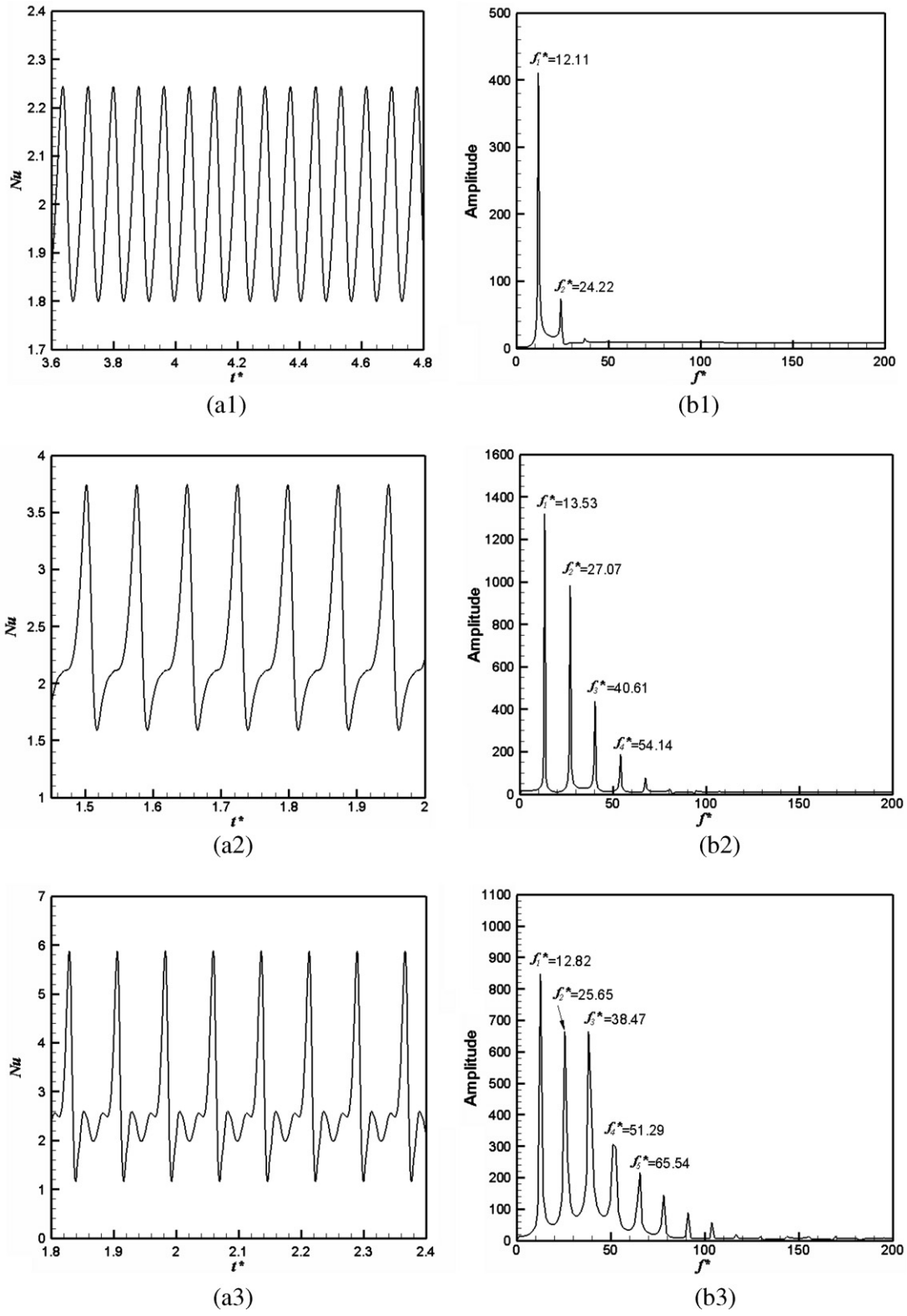

Fig. 8. FFT spectrum analysis results for oscillatory unstable flows at mesoscopic scale ($Kn = 10^{-2}$) in cavity with aspect ratio of AR = 2.0, $Pr = 0.71$, and various Ra^*: (a1) variation of Nusselt number with dimensionless time-step at $Ra^* = 6.5 \times 10^3$, (a2) variation of Nusselt number with dimensionless time-step at $Ra^* = 10^4$, (a3) variation of Nusselt number with dimensionless time-step at $Ra^* = 1.5 \times 10^4$, (a4) variation of Nusselt number with dimensionless time-step at $Ra^* = 1.8 \times 10^4$, and (a5) variation of Nusselt number with dimensionless time-step at $Ra^* = 2 \times 10^4$; (b1) relationship between dimensionless frequency and oscillatory amplitude at $Ra^* = 6.5 \times 10^3$, (b2) relationship between dimensionless frequency and oscillatory amplitude at $Ra^* = 10^4$, (b3) relationship between dimensionless frequency and oscillatory amplitude at $Ra^* = 1.5 \times 10^4$, (b4) relationship between dimensionless frequency and oscillatory amplitude at $Ra^* = 1.8 \times 10^4$, and (b5) relationship between dimensionless frequency and oscillatory amplitude at $Ra^* = 2 \times 10^4$.

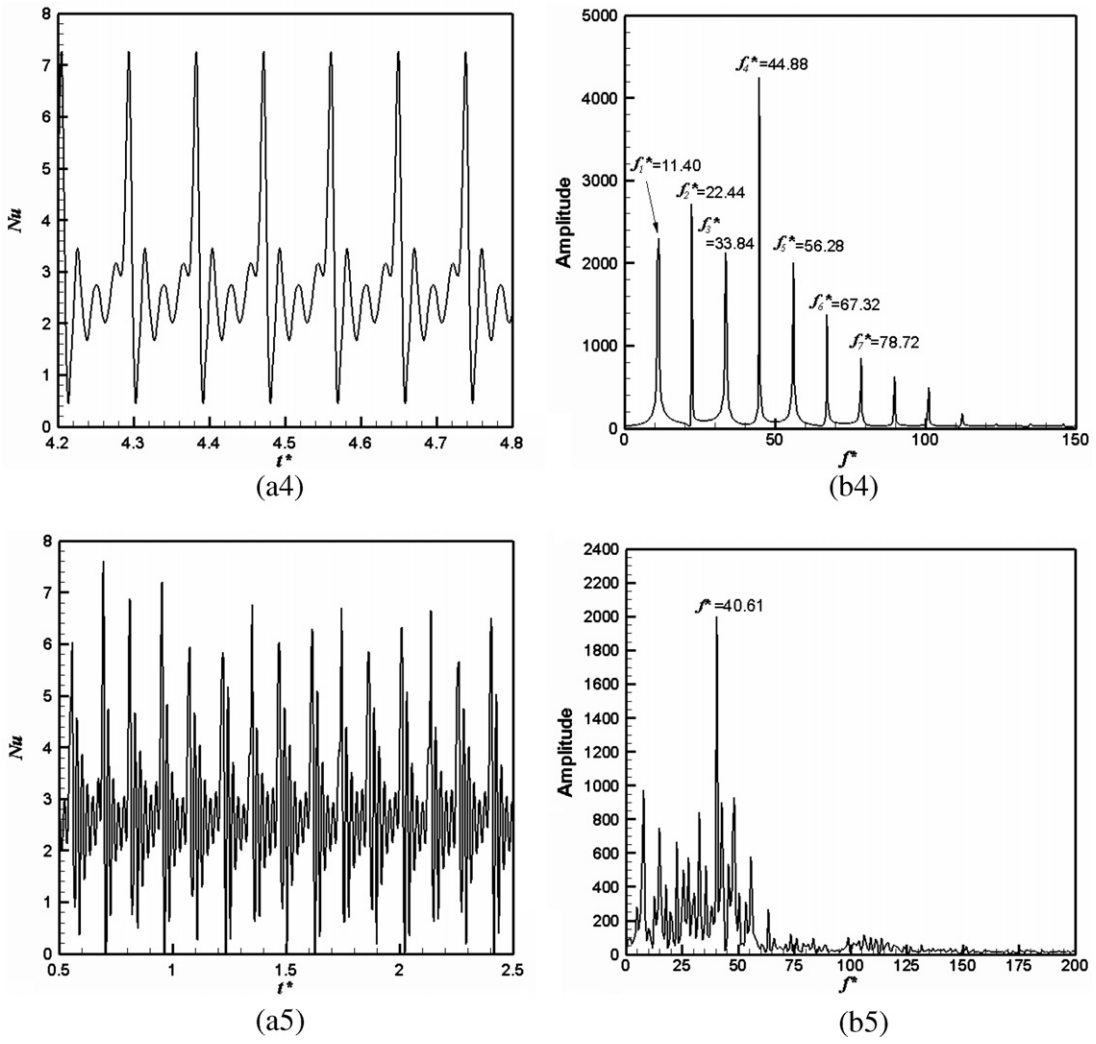

Fig. 8 (*continued*)

10^4. It can be seen that the Nusselt number varies as a function of the Rayleigh number, the Knudsen number, and the cavity aspect ratio at both scales. In general, the results indicate that the Knudsen number has a significant effect in inducing secondary unstable flow, but has little effect on the onset of primary instability. For a constant aspect ratio, a larger value of the Knudsen number (i.e. $Kn = 10^{-2}$) induces unstable oscillatory flow (i.e. secondary instability) at a lower Rayleigh number. Although the onset of secondary instability is also dependent on the aspect ratio of the cavity, the results suggest that the effect of the Knudsen number is more dominant. In other words, the Knudsen number has a greater effect on the heat transfer characteristics of the natural convection system within the closed cavity than the aspect ratio in the present simulations.

Fig. 10 shows that a higher value of the Knudsen number ($Kn = 10^{-2}$) has a significant effect on the flow structure and yields a slight improvement in the heat transfer effect with increasing AR and Ra^*. From inspection, the computed values of the Nusselt number at the mesoscopic scale are slightly higher than those at the macroscopic scale when the flow is in a stationary state. However, following the onset of secondary instability with an oscillatory flow, the values of the Nusselt number at the mesoscopic scale are lower than those without secondary instability computed at the macroscopic scale for a given Ra^* value. In other words, it can be inferred that the unsteady unstable flow associated with secondary instability may not yield a significant improvement in the heat transfer of natural convection systems within closed cavities.

Finally, in order to ensure the LB simulations in present study are performed within the incompressible regime, the maximum Mach number is checked by calculating $Ma \approx \langle u_y \rangle / c_s$ at $Ra = 2 \times 10^4$ and $Kn = 10^{-2}$ for every aspect ratio, i.e. AR = 0.5, 1.0, 1.5, and 2.0, respectively. The result exhibited that the maximum Mach number was in the order of 10^{-3}, which is much smaller than the limit of $Ma < 0.3$. Therefore, the flow is within the incompressible regime.

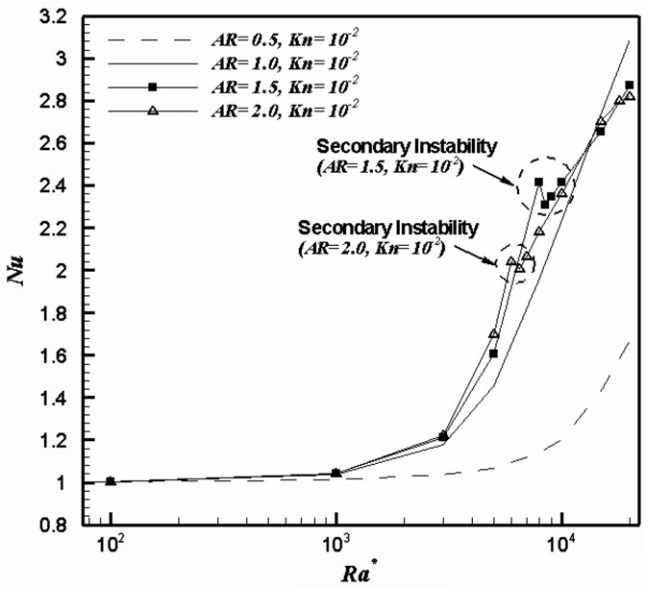

Fig. 9. Variation of Nusselt number with reference Rayleigh number at mesoscopic scale ($Kn = 10^{-2}$) for cavities with aspect ratios in the range $0.5 \leqslant \mathrm{AR} \leqslant 2.0$, $Pr = 0.71$, and $Ra^* \leqslant 2 \times 10^4$.

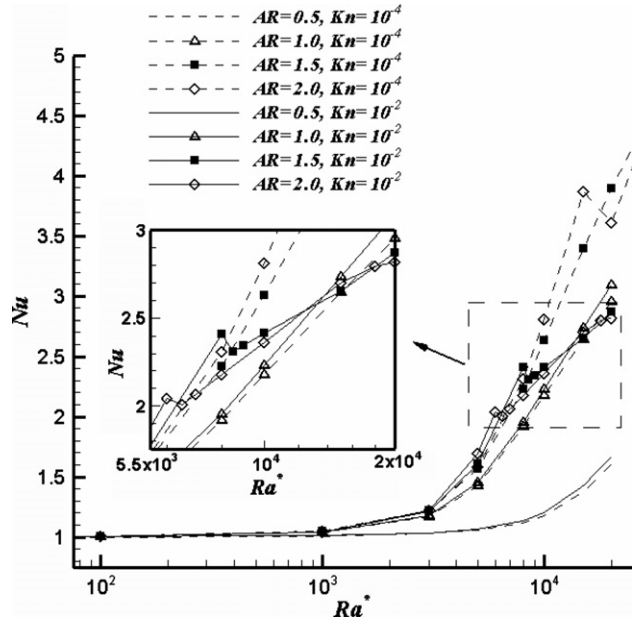

Fig. 10. Comparison of solutions obtained at the macroscopic scale ($Kn = 10^{-4}$) and the mesoscopic scale ($Kn = 10^{-2}$), respectively, for variation of Nusselt number with reference Rayleigh number for cavities with aspect ratios in the range $0.5 \leqslant \mathrm{AR} \leqslant 2.0$, $Pr = 0.71$, $Ra^* \leqslant 2 \times 10^4$.

5. Conclusions

In general, the present simulation results have shown that the flow structures generated in a natural convection within a closed cavity are strongly dependent on the Knudsen number, the Rayleigh number, and the aspect ratio of the cavity. Specifically, the primary instability is generated at a critical Rayleigh number of approximately $Ra_c = 10^3$–10^4 irrespective of the Knudsen number. Meanwhile, the cavity aspect ratio also seems insensitive relatively to the critical Rayleigh number for primary instability. However, the bifurcation to secondary instability takes place only at certain aspect ratios, and Knudsen numbers, and reference Rayleigh numbers, respectively, i.e. $Ra^* = 1.5 \times 10^4$–2×10^4 for $\mathrm{AR} = 2.0$ at the macroscopic scale ($Kn = 10^{-4}$), and $Ra^* = 8 \times 10^3$–8.5×10^3 for $\mathrm{AR} = 1.5$ and $Ra^* = 6 \times 10^3$–6.5×10^3 for $\mathrm{AR} = 2.0$ at the mesoscopic scale ($Kn = 10^{-2}$). In other words, the formation of secondary instability flow is determined primarily by the Knudsen number and the aspect ratio of the cavity. Once the threshold of secondary instability is exceeded, a bifurcation to a single-frequency periodic oscillatory flow with a symmetry-breaking structure may be observed. As the value of the Rayleigh number increases, harmonic frequencies are induced via the frequency doubling route ($f_N^* = f_1^* \cdot N$). However, as the Rayleigh number is increased further, the number of harmonic frequencies or flow perturbations is then induced, causing the doubly harmonic frequencies relationship to be broken and the flow finally transitions to a near-chaotic state.

Regarding the relationship between the Nusselt number and the reference Rayleigh number, the results show that unsteady unstable flow fails to provide an effective enhancement in the heat transfer performance of the natural convection system when the system is confined within a cavity with a high aspect ratio, e.g. the results shown in Fig. 9 at the mesoscopic scale. Overall, the results of the flow sequence from stationary unstable flow to periodic oscillatory flow presented in this study for the macroscopic scale ($Kn = 10^{-4}$) with $\mathrm{AR} = 1.5$ and 2.0 are in good qualitative agreement with those reported in previous studies [3,4]. Furthermore, the current results demonstrate the importance of the Knudsen number, which represents the characteristics of the flow depend on the length scale of interest (e.g. at the macroscopic or mesoscopic scale), when investigating natural convection problems.

The LB model employed in this study provides a straightforward means of simulating the instability characteristics of natural convection with complicated nonlinear physics at both the macroscopic and mesoscopic scaled. The results presented in this study provide useful insights into the formation of primary instability in natural convection systems, the subsequent transition to secondary instability, and the flow structures associated with each regime. In addition, the simple model proposed for determining appropriate values of the buoyant characteristic velocity provides a convenient and reliable tool for LB simulations of natural convection at the macroscopic or mesoscopic scale.

To enable the simulation of natural convection systems with higher Rayleigh numbers or in the fully-turbulent regime, respectively, future studies would apply the interpolation supplemented lattice Boltzmann method (ISLBM) presented in [15] and the multi-relaxation time (MRT) method. Furthermore, a more robust thermal LB model

will be developed which takes into account the effects of viscous thermal dissipation and utilizes an appropriate turbulence model.

References

[1] G. de Vahl Davis, Natural convection of air in a square cavity: a bench mark numerical solution, Int. J. Numer. Methods Fluids. 3 (1983) 249–264.

[2] S. Ostrach, Natural convection in enclosures, J. Heat Trans., 50th Anni. Issue 110 (1988) 1175–1189.

[3] C. Xia, J.Y. Murthy, Buoyancy-driven flow transitions in deep cavities heated from below, Trans. ASME 124 (2002) 650–659.

[4] D.W. Crunkleton, R. Narayanan, T.J. Anderson, Numerical simulations of periodic flow oscillations in low Prandtl number fluids, Int. J. Heat Mass Transfer 49 (2006) 427–438.

[5] O. Aydin, A. Ünal, T. Ayhan, Natural convection in rectangular enclosures heated from one side and cooled from the ceiling, Int. J. Heat Mass Transfer 42 (1999) 2345–2355.

[6] M.M. Ganzarolli, L.F. Milanez, Natural convection in rectangular enclosures heated from below and symmetrically cooled from the sides, Int. J. Heat Mass Transfer 38 (1995) 1063–1073.

[7] A. Dalal, M.K. Das, Natural convection in a rectangular cavity heated from below and uniformly cooled from the top and both sides, Numer. Heat Transfer Part A 49 (2006) 301–322.

[8] M.A.R. Sharif, T.R. Mohammad, Natural convection in cavities with constant flux heating at the bottom wall and isothermal cooling from the side wall, Int. Therm. Sci. 44 (2005) 865–878.

[9] S. Chen, G.D. Doolen, Lattice Boltzmann method for fluid flows, Annu. Rev. Fluid Mech. 30 (1998) 329–364.

[10] D. Yu, R. Mei, L.S. Luo, W. Shyy, Viscous flow computations with the method of lattice Boltzmann equation, Progr. Aerospace Sci. 39 (2003) 329–367.

[11] S. Succi, The Lattice Boltzmann Equation for Fluid Dynamics and Beyond, Clarendon Press, Oxford, 2001.

[12] X. Shan, Simulation of Rayleigh–Bénard convection using a lattice Boltzmann method, Phys. Rev. E 55 (1997) 2780–2788.

[13] X. He, S. Chen, G.D. Doolen, A novel thermal model for the lattice Boltzmann method in incompressible limit, J. Comput. Phys. 146 (1998) 282–300.

[14] Y. Zhou, R. Zhang, I. Staroselsky, H. Chen, Numerical simulation of laminar and turbulent buoyancy-driven flows using a lattice Boltzmann based algorithm, Int. J. Heat Mass Transfer 47 (2004) 4869–4879.

[15] H.N. Dixit, V. Babu, Simulations of high Rayleigh number natural convection in a square cavity using the lattice Boltzmann method, Int. J. Heat Mass Transfer 49 (2006) 727–739.

[16] P.-H. Kao, R.-J. Yang, Simulating oscillatory flows in Rayleigh–Bénard convection using the lattice Boltzmann method, Int. J. Heat Mass Transfer 50 (2007) 3315–3328.

[17] Y. Peng, C. Shu, Y.T. Chew, Simplified thermal lattice Boltzmann model for incompressible thermal flows, Phys. Rev. E 68 (2003) 026701.

[18] G. Barrios, R. Rechtman, J. Rojas, R. Tovar, The lattice Boltzmann equation for natural convection in a two-dimensional cavity with a partially heated wall, J. Fluid Mech. 522 (2005) 91–100.

[19] Y.H. Qian, D. d'Humieres, P. Lallemand, Lattice BGK models for Navier–Stokes equation, Europhys. Lett. 17 (6) (1992) 479–484.

[20] Y.H. Qian, S.A. Orszag, Lattice BGK models for the Navier–Stokes equation: non-linear deviation in compressible regimes, Europhys. Lett. 21 (1993) 255–259.

[21] S.P. Dawson, S. Chen, G.D. Doolen, Lattice Boltzmann computations for reaction–diffusion equations, J. Chem. Phys. 98 (1993) 1514–1523.

[22] C. Cercignani, Mathematical Methods in Kinetic Theory, Plenum, New York, 1969.

[23] G. Wannier, Statistical Physics, Diver, New York, 1966.

[24] C. Shu, X.D. Niu, Y.T. Chew, A lattice Boltzmann kinetic model for microflow and heat transfer, J. Stat. Phys. 121 (1–2) (2005) 239–255.

[25] Y. Peng, C. Shu, Y.T. Chew, A 3D incompressible thermal lattice Boltzmann model and its application to simulate natural convection in a cubic cavity, J. Comput. Phys. 193 (2003) 260–274.

[26] E.J. Braga, M.J.S. de Lemos, Heat transfer in encloses having a fixed amount of solid material simulated with heterogeneous and homogeneous models, Int. J. Heat Mass Transfer 48 (2005) 4748–4765.